PAPER • OPEN ACCESS

Beam test performance of a prototype module with Short Strip ASICs for the CMS HL-LHC tracker upgrade

To cite this article: The Tracker Group of the CMS collaboration]Corresponding author: Marc Osherson. *et al* 2022 *JINST* **17** P06039

View the article online for updates and enhancements.

Beam test performance of a prototype module with Short Strip ASICs for the CMS HL-LHC tracker upgrade

The Tracker Group of the CMS collaboration

E-mail: marc.osherson@cern.ch

ABSTRACT: The Short Strip ASIC (SSA) is one of the four front-end chips designed for the upgrade of the CMS Outer Tracker for the High Luminosity LHC. Together with the Macro-Pixel ASIC (MPA) it will instrument modules containing a strip and a macro-pixel sensor stacked on top of each other. The SSA provides both full readout of the strip hit information when triggered, and, together with the MPA, correlated clusters called stubs from the two sensors for use by the CMS Level-1 (L1) trigger system. Results from the first prototype module consisting of a sensor and two SSA chips are presented. The prototype module has been characterized at the Fermilab Test Beam Facility using a 120 GeV proton beam.

Corresponding author: Marc Osherson.

Contents

1   Introduction

The Large Hadron Collider (LHC) will be upgraded to operate at increased instantaneous luminosities of up to $7.5 \times 10^{34}\,\mathrm{cm^{-2}s^{-1}}$, which will result in up to 200 proton-proton interactions per bunch crossing, with the goal of accumulating a total integrated luminosity of $3\,\mathrm{ab^{-1}}$ [1]. The CMS detector [2] will be upgraded [3, 4] to handle these new data-taking conditions. The current CMS trigger system [5] consists of the Level-1 (L1) trigger, instrumented by custom hardware processor boards, and a software High Level Trigger (HLT). The current L1 trigger receives information from detector sub-systems and performs an initial selection within a fixed latency of 4 μs, with a maximum output rate of 100 kHz. When an event is selected by the L1 trigger, the detector is fully read out to the HLT system, where a final decision is made on whether to store the event. The new L1 trigger system will use a latency of up to 12.5 μs and will be capable of sustaining an L1-accept rate of 750 kHz.

The entire CMS silicon tracker will need to be replaced for the High Luminosity LHC era. The current tracker [2, 6], composed of pixel and strip tracking systems, will be replaced by two related detectors: the Inner Tracker (IT) and the Outer Tracker (OT), shown in figure 1. This new tracker will have increased radiation tolerance, with the innermost layer of the IT (OT) able to handle the

expected 1 MeV neutron equivalent fluence of 2.3×10^{16} (9.6×10^{14}) n_{eq}/cm^2, for a total expected ionizing dose of $12\,(0.56)$ MGy. In addition, the new tracker will have increased granularity to ensure efficient tracking performance despite the higher particle rates and densities, including a new tracking capability for the L1-trigger [3]. The OT will use two types of modules (2S and PS), each consisting of two silicon sensors forming closely spaced parallel planes. Correlated clusters from high transverse momentum tracks are identified using on-chip logic and form Level-1 trigger primitives (stubs), as shown in figure 2.

The 2S modules, positioned at outer radii where the particle occupancy will be lower, are comprised of two strip sensors read out by the CMS Binary Chip (CBC3) ASIC described in refs. [7, 8]. The PS modules, shown in figure 3, are situated closer to the beam pipe and consist of macro-pixel (100 μm pitch × 1460 μm length) and short strip (100 μm pitch × 25 mm length) sensors, with the strips intended to be parallel to the beam direction. The Macro-Pixel ASICs (MPA) [9] are bump-bonded to the former, while the latter is wire-bonded to a hybrid and is read out by the Short Strip ASIC (SSA) [10, 11] bump-bonded to the same hybrid. A module is read out by sixteen SSAs and MPAs, with a pair of Concentrator Integrated Circuits (CICs) [12] responsible for aggregating their returned data. The Low-power Gigabit Transceiver (LpGBT) [13] distributes clock, trigger and control signals to the eight SSAs and eight MPAs on each side of the module. The SSA is also capable of flagging hits from Highly Ionizing Particles (HIPs) by discriminating the hit amplitude against a programmable threshold. This flag can be combined with data from other sub-detectors in CMS to increase the sensitivity of analyses seeking to identify such particles. The SSA also performs strip hit clustering and transmits the clusters to the MPA to be used for stub formation.

This paper describes the first prototype detector module consisting of a sensor with the same strip configuration as in the final detector and two SSA chips. The module was built in 2019 and tested in January 2020 at the Fermilab Test Beam Facility, with the primary goal of verifying the chip front-end performance.
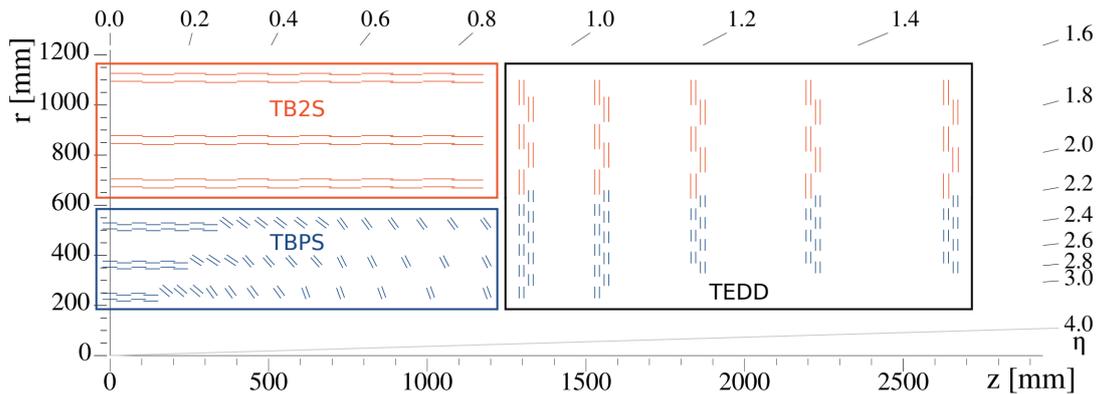

Figure 1. Sketch of a slice of one quarter of the Outer Tracker in the longitudinal view [4]. The CMS coordinate system is centered on the nominal collision point. The z direction points along the beam axis. The polar angle measured with respect to the z direction is denoted by θ, though the pseudorapidity $\eta = -\ln\tan(\theta/2)$ is often used instead. PS modules are indicated in blue, 2S modules in red. The tracker barrel with 2S and PS modules (TB2S and TBPS) and the tracker endcap double-discs (TEDD) are shown.
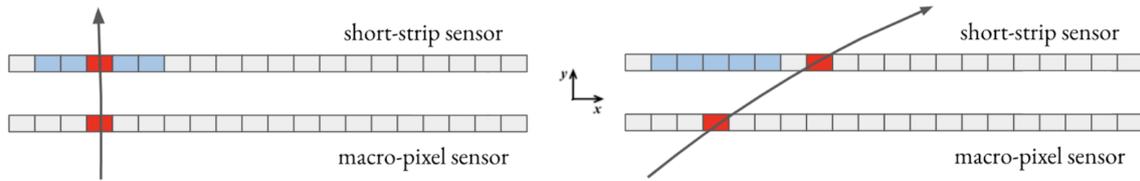
Figure 2. Diagram of stub formation in the PS module: high momentum particles (left) are less affected by the 3.8 T magnetic field created by the CMS solenoid than a low momentum particle (right), whose trajectory is significantly bent by the field. Simultaneous hits (or clusters of hits) recorded by the MPA and SSA only form a stub if the hits in the SSA are within a programable fiducial region (shown in blue) of the short strip sensor, seeded by the location of the hit in the macro-pixel sensor. Conceptually, the stub formation in the 2S modules is similar to that for the PS module shown here.
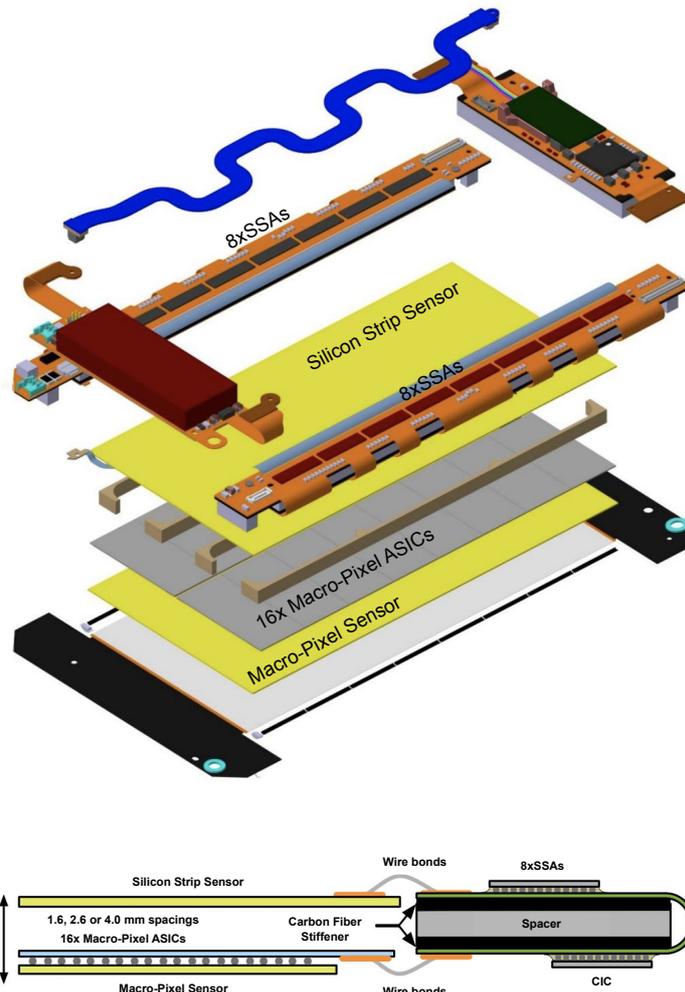
Figure 3. (Top) Drawing of the exploded view of the PS module (updated from ref. [4]). Key components are: the strip sensor (yellow), MPAs (grey) and the macro-pixel sensor in the central part of the module. The strip sensor is wire-bonded to a hybrid and is read out by the SSAs, which are bump-bonded to the same hybrid. (Bottom) Drawing showing the cross-sectional view of a PS module, including wire-bond connections, supporting structures and the CIC which aggregates the returned data from 8 SSAs and 8 MPAs.

The paper first describes the SSA chip, the 2×SSA module under test, and the experimental setup at the test beam facility. A simulation of the expected performance of the module is described, as is the procedure by which this model was tuned. Finally, measurements of the module timing and the hit reconstruction efficiency, cluster size and resolution at different incident angles are presented and the agreement between data and simulation is studied.

2 The Short Strip ASIC

The SSA, fabricated in 65 nm CMOS technology, is described in detail in ref. [10]. Each SSA chip can read out 120 channels from a short strip sensor. After amplification and signal shaping in the analog front-end, signals are discriminated with a double threshold binary system: one for the L1 hit data (detection threshold) and one for the HIP flagging (HIP threshold). These thresholds can be programmed, and are typically set to detect hits with charge consistent with 1/4 of the energy deposited by a minimum ionizing particle (MIP) energy (a signal of approximately $4.5 \, \text{ke}^-$) for the detection threshold, and 1.4 MIPs (approximately $25 \, \text{ke}^-$) for the HIP threshold. The SSA can be programmed to digitize both signals using either an edge-sensitive or level-sensitive circuit, sampling at 40 MHz (the exclusive "or" of the two modes can also be used). In order to maximize the hit detection efficiency, the sampling clock phase is coarsely adjustable in steps of 3.125 ns across the full 25 ns bunch crossing period, with an additional fine adjustment in steps of 200 ps. The hits are transmitted via two data paths: the stub data path and the L1 path. The stub data path carries up to eight centroids (either the position of single hits or the center of a cluster of neighboring hits) which are passed to the MPA in the PS module for momentum discrimination. The L1 path stores the hit status of all channels until they are requested by the trigger system, with latencies of up to 12.8 μs. In the PS module, the L1 data are also transmitted to the MPA, which forms clusters and transmits them (along with the clusters from the pixel layer) when triggered to the HLT. In addition, the eight leftmost and rightmost strip signals can be transmitted to adjacent SSAs using so-called "lateral" communication lines (allowing the PS module to deal with clusters whose hits are recorded on two adjacent SSAs). All results in this paper are based on the triggered (L1) data path. A data-flow diagram for the SSA and MPA combination, as intended for use in the full PS module, is shown in figure 4.

3 Experimental setup

Validation of the PS module, including studies of the synchronization, efficiency and resolution, are being performed on prototypes which seek to isolate the performance of individual ASICs. In the case of the SSA, the device under test (DUT) is referred to as the 2×SSA module, and consists of a strip sensor connected to two SSA chips. This module was tested in a proton beam where the trajectories of the incoming protons were measured and exploited to characterize the behavior of the 2×SSA module.

3.1 2×SSA module

The DUT (shown in figure 5) consists of a single, 240 channel n-in-p Float Zone silicon sensor [14] with each channel wire-bonded to one of two sapphire interposers which were in turn each bump-
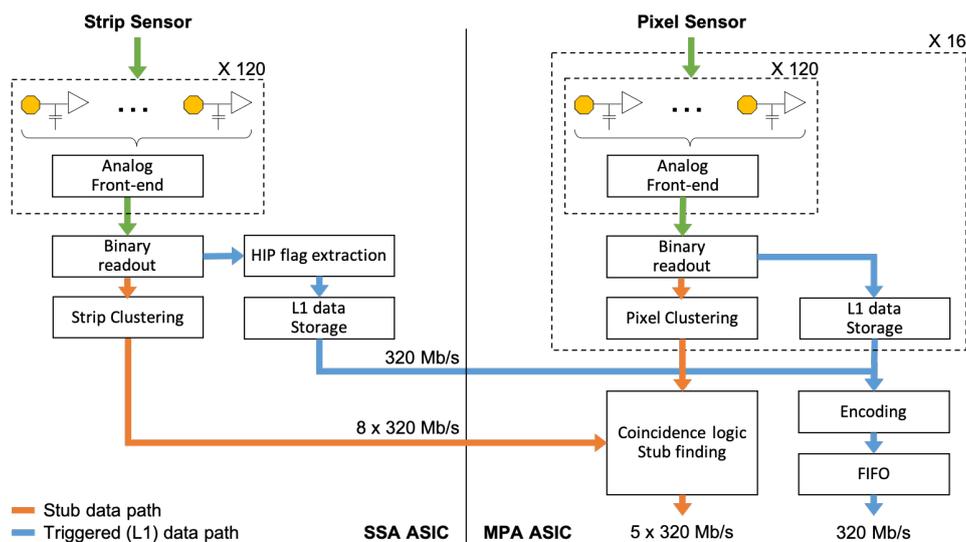
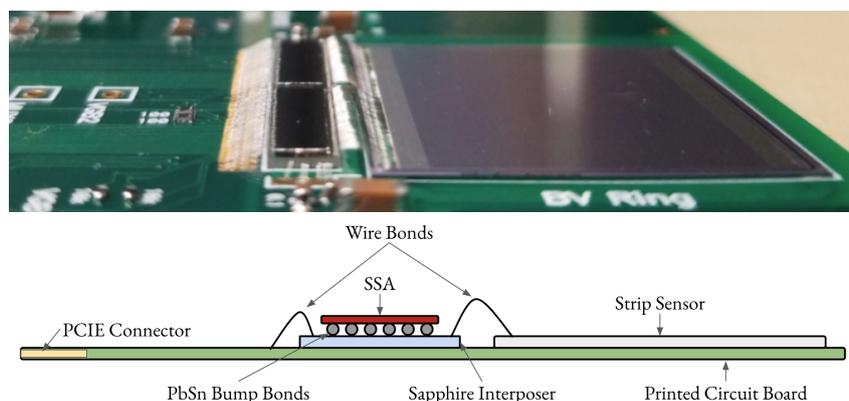**Figure 4**. Data-flow diagram for the PS module, showing both the SSA and MPA readout functionality.

Figure 5. (Top) A close-up picture of the DUT. From right to left: the silicon sensor (large gray square), wire-bonds connecting it to the interposers, the SSA chips (two small dark rectangles), wire-bonds connecting the interposer to the printed circuit board. The interposers are located beneath each SSA, and are not visible in this image. (Bottom) A diagram of the 2×SSA module. The SSAs are bump-bonded (PbSn) to the sapphire interposers. The prototype module has a similar configuration to how the eventual PS modules will be constructed. Power, communication and data lines are passed to the SSAs from the PCB through the wire-bonds and bump-bonds. High voltage to bias the sensor is transmitted through the printed circuit board.

bonded to an SSA chip (mimicking the eventual configuration in the PS module). The sensor has a strip pitch of 100 μm and a length of 23 mm. The active sensor thickness is 240 μm, with minimal additional inactive thickness (1 μm). The sensor is read out by two SSAs, with the boundary between the 120 channels connected to each chip located at the center of the sensor. To ensure full depletion of the silicon, the sensor was biased to −350 V for all results presented here. Each chip's lateral data lines are connected to the other chip; this feature was used to verify the functionality of these lateral lines, but is not used in any aspect of the data processing from this beam test. The SSAs were operated in the edge-sensitive mode.

Individual channels of the front-ends may respond differently for a nominal threshold setting (due for example to process variations in the lithography of the ASICs). To account for this, every SSA channel's discriminator is individually adjustable with a configurable offset. To ensure an even response across all channels, these are tuned using a known signal: calibration pulses from the discharge of on-chip 52 fF capacitors on each channel. The DC level of this calibration line is controllable, and can be tuned against an external reference. This tuning of individual channels is not available for the HIP signals.

3.2 Test Beam parameters

The Fermilab Test Beam Facility receives a beam of protons at an energy of 120 GeV from the Fermilab Main Injector. These protons are delivered in a long spill of 4.2 seconds, once per minute, with between 100 000 and 200 000 particles per spill. A picture of the experimental setup with the DUT, as well as the relevant coordinate system, is shown in figure 6. The test beam facility is equipped with a silicon tracking telescope [15] to precisely measure the paths of incoming particles. The telescope is composed of seven silicon strip planes, alternating between horizontal and vertical orientation, with a strip pitch of 60 μm, and four silicon pixel planes composed of 100 μm × 150 μm pixels. It covers an active area of approximately 1.4 cm × 1.4 cm at the DUT. The impact resolution at the DUT was measured to be less than 15 μm. A common clock approximating the needed 40 MHz clock is provided to both the DUT and the telescope, and is obtained by multiplying the accelerator clock of 53 MHz by a factor of 3/4 (for a true clock rate of 39.75 MHz with 25.15 ns cycles). This is done so that the phases between the proton arrival, telescope and DUT clocks remain fixed.

The telescope and DUT are simultaneously triggered by a scintillator detector with a time resolution of a few hundred picoseconds. When triggered, the telescope outputs full three-dimensional information on all tracks in a given clock cycle. During the beam test, the DUT, with strips oriented vertically (y), was placed down-stream of the first four strip planes, followed by a further three strip and four pixel planes. This configuration places the DUT amongst the strip planes, which have a better resolution. The DUT was fixed to a table which can move along and rotate about the x and y axes.

3.3 Data acquisition

The DUT's data acquisition system is built around the FC7 card [16], a specialized μTCA compatible Advanced Mezzanine Card (AMC) equipped with a Kintex 7 FPGA. The FC7 communicates with both SSA chips through a custom FPGA Mezzanine Card (FMC). The DUT is electrically connected to the FMC via a custom made interface board, which also relays power to the DUT. Commands are sent through the interface board to the DUT following the I2C protocol and through a dedicated fast command line which sends the trigger accept signals. The module sends signals to the FC7 through a total of seventeen SLVS lines. Fifteen of these lines are used for the cluster centroids which are sent on each DUT clock cycle (the sixteenth line is left unconnected due to insufficient connections on the interface card). The remaining two lines are used for the L1 data of each chip, and only send data when the DUT is triggered. The triggers and the shared clock are input to the FC7 via a second FMC, and passed on to the DUT. The FPGA firmware implementation is specific to the 2×SSA module, and is controlled and read out via IPBus by the Phase-2 Acquisition and Control Framework (Ph2 ACF) [17, 18] developed for the Tracker Upgrade program.
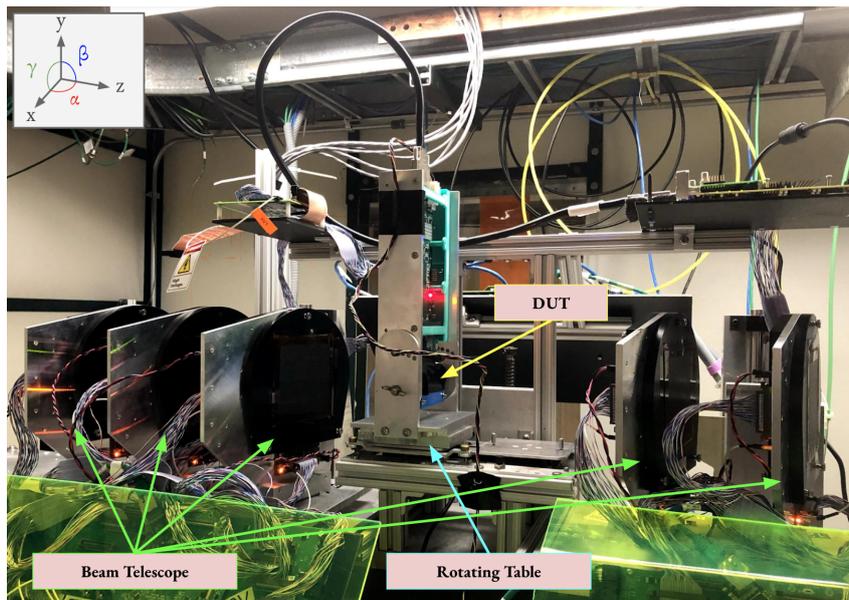
Figure 6. Experimental setup at the Fermilab Test Beam Facility. The DUT was placed on a rotating table at the center of the silicon tracking telescope (only five of the seven silicon planes are shown in the picture). The beam travels from left to right along the axis marked *z*.

The telescope is controlled and read out using the "Off the Shelf" data acquisition program (OTSDAQ), which is based on *artdaq* [19] and is maintained by Fermilab. The data from both the telescope and DUT are processed with the Monicelli software package for track reconstruction and alignment [15].

4   Simulations

In section 5 we compare the performance of the DUT measured at the test beam to a simple model of the sensor whose parameters are fit to the data to improve the quantitative understanding of the observations. The goal of the model is to predict the amount of charge collected in each strip of the sensor for different interstrip positions (x) and incident angles (θ) of the incoming protons. The parameters of the model are fit to the measurements of the efficiencies and cluster sizes for different values of the DUT horizontal rotation angle α (as defined in figure 6). The model assumes an effective depleted region of $d_{\text{eff}} = \min(d_0, d_0\sqrt{U_{\text{b}}/U_{\text{fd}}})$, with a sensor thickness $d_0 = 240\,\mu\text{m}$, a depletion voltage $U_{\text{fd}} = 250\,\text{V}$, and supply voltage U_{b}. The probability density distribution of electron-hole pairs produced by a proton entering the silicon sensor is assumed to follow a Landau distribution [20], and is modeled in the simulation with an approximation as described in ref. [21]. The most probable value (μ) and width (σ) parameters of the distribution are considered free parameters of the model. The charge is increased to μ × $1/\cos\theta$ to account for the incident angle. When the proton crosses an active area covered by multiple strips, the charge is divided between the strips proportional to the distance traversed in each strip.

Two additional effects are taken into account: diffusion of charge along the trajectory of the proton, and capacitive coupling between the strips. Close to the edges between two strips charges

Table 1. Parameters and their uncertainties of the simple model obtained from a fit of the measurements of the efficiencies and cluster sizes for different horizontal rotation angles α between $0°$ and $18°$.

Parameter	Value
Landau μ	$(20.6 \pm 0.2)\,\text{ke}^-$
Landau σ	$(1.8 \pm 0.1)\,\text{ke}^-$
σ_{diff}	$(2.8 \pm 0.5)\,\mu\text{m}$
f_{x}	$(9.3 \pm 0.2)\%$

may diffuse across the strip boundaries, where the fraction of the charge ΔQ that is lost along a path element Δs and observed in the adjacent strip increases as the position approaches the edge. This fraction is described by the integral function of a Gaussian distribution (the Erf). Its width σ_{diff} describes the size of the diffusion region, and is a free parameter of the model. The effect of induced signals in strips adjacent to the actual traversed strip due to the capacitive coupling between strips (charge sharing) is simulated by subtracting a certain fraction of the expected charge in the traversed strip and adding it to the adjacent strip. This fraction f_{x} is another parameter of the model.

Finally, after the charges are calculated in all strips they are modulated by a Gaussian distribution to simulate the combined noise from the SSAs and sensor. This term is added for each strip individually, but is measured by averaging the noise in all strips in the DUT. The noise was measured after the DUT was installed at the Test Beam Facility, prior to receiving beam, and is found to be about $830\,\text{e}^-$. Taking all these components, the total charge collected by a strip A, when the sensor is traversed by the proton along a path S which also crosses strip B, is given by:

$$Q_{\text{tot,A}} \approx (1 - f_{\text{x}}) \int_S \frac{\{L\}}{S} \, \text{Erf}\left(\frac{x - x_e}{\sqrt{2}\sigma_{\text{diff}}}\right) ds + f_{\text{x}} \int_S \frac{\{L\}}{S} \, \text{Erf}\left(\frac{x_e - x}{\sqrt{2}\sigma_{\text{diff}}}\right) ds + \{\mathcal{N}\} \quad (4.1)$$

where $\{L\}$ is sampled from the Landau distribution with most probable value μ and width σ, and x_e is the position of the boundary between strips A and B. The noise $\{\mathcal{N}\}$ is sampled from a Gaussian distribution with a mean of 0 and a width of $830\,\text{e}^-$. Additional terms could be added for other adjacent strips, but these effects are negligible.

The four extracted parameters are summarized in table 1. Notably, the post-fit value of μ is $20.6\,\text{ke}^-$, close to the expected value of $19\,\text{ke}^-$ for a $120\,\text{GeV}$ proton in $240\,\mu\text{m}$ of silicon.

5 Analysis

5.1 Hit clustering

Many of the subsequent analyses use clusters, which are formed by contiguous hits in multiple adjacent strips. The position of a cluster is calculated as the average position of the constituent strips. The studies presented in this paper use clusters reconstructed after data-taking from the L1 hit outputs of the DUT. This allows the analysis to consider the number of strips in each cluster, rather than just the positions output by the SSAs' stub data lines. With this definition, cluster positions can be in the middle of two strips. The centroids from the DUT's stub data were verified to be in agreement with this offline reconstruction. For a threshold of $6.2\,\text{ke}^-$ (1 fC), a sensor bias voltage $U_{\text{b}} = -350\,\text{V}$, and all rotational angles at zero, 90% of the clusters consist of a single strip and 9% of two strips. At this
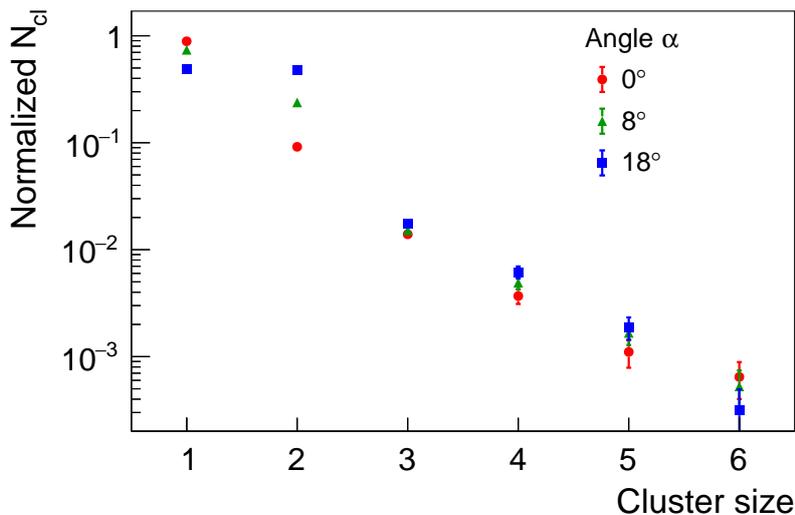
Figure 7. Fraction of clusters N_{cl} as function of the cluster size (number of strips) for three horizontal rotational angles α. Each distribution is normalized to unity.

detection threshold, the strip occupancy from noise across the entire module is approximately 0.0025%. The distributions of number of clusters N_{cl} as a function of the cluster size for three different rotational angles α are shown in figure 7, and we see that the average cluster size increases for higher angles.

5.2 Alignment

The first step of the analysis is the calibration of the position and orientation of the DUT with respect to the track trajectories determined by the beam telescope. The goal of this alignment is the calculation of the particle track positions at the surface of the DUT and, consequently, the identification of tracks that do not traverse the sensor of the DUT.

Six parameters are considered in the alignment, including the transverse horizontal x and vertical y positions of the origin of the DUT reference frame at the upper left corner of the sensor surface, and its z position parallel to the beam axis. In addition, there are three rotation angles of the DUT reference frame: a rotation angle γ around the z axis; the horizontal rotation angle α around the y axis; and finally the vertical rotation angle β around the x axis (all angles are shown in figure 6). These parameters are initialized with approximate values obtained from the measured experimental settings and then determined precisely using the tracks from the beam telescope as follows. We calculate the residual between a track (modeled as a straight line) and the closest cluster centroid. The sum of these distances squared is minimized for each configuration of the DUT. The information of the strips is not sufficient to constrain all parameters necessary for an absolute three-dimensional positioning of the DUT. The vertical rotation β cannot be obtained from the information of the strips. Any deviation from the assumed value of 0° would result in an effective sensor thickness slightly above the nominal 240 µs. The y position (in the DUT reference frame) can only be constrained if the beam partially crosses the upper or lower edge of the DUT surface. Since the tracks are almost parallel to the beam axis, the z position becomes arbitrary.
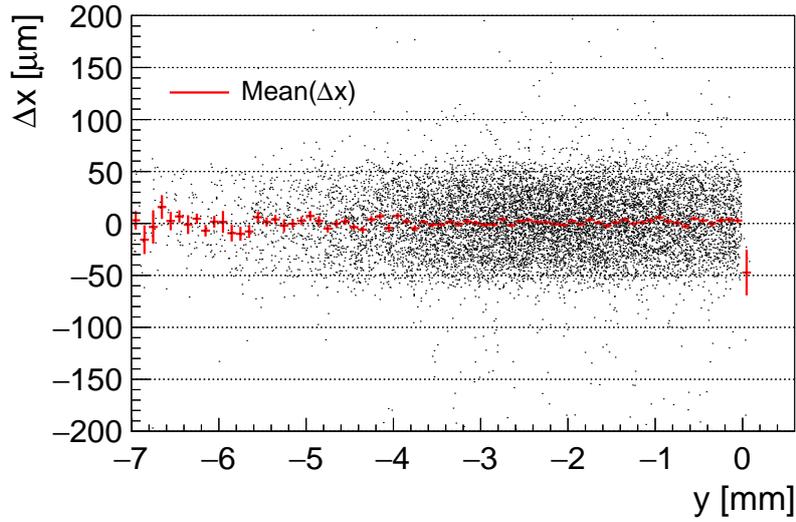
Figure 8. Distribution of the residuals (Δx) between track position and closest cluster centroid as a function of the y position measured by the telescope, for each event. The residual distribution has no dependence on the vertical position y, confirming a successful alignment. The average values of the residuals as a function of the y position is shown in red.

In figure 8 the residuals of the track positions at the DUT (after the alignment procedure) and the cluster centroid (Δx) are shown as a function of the y position measured with the telescope. Since there is no dependence of Δx as a function of the y position, this confirms a successful alignment of the rotation angle γ around z.

5.3 Timing efficiency

The SSA stores the full hit information for each clock cycle in an internal buffer for up to 12.8 μs. Within this period a trigger decision should be made if the full hit data is to be read out and stored. Since the processing and distribution of the trigger signal to the DUT takes some time (latency), the correct corresponding entry from the DUT's internal buffer must be selected. In addition, since the digitization of the collected charge by the analog front-end circuit is not instantaneous, the arrival time of the proton within a clock cycle can affect the reconstruction efficiency. In the extreme case, the signal from charge collected in the strip does not reach the threshold needed to indicate a hit within the 25 ns window selected in the buffer (in such cases the hit would appear in the next window). The effect is especially pronounced when the charge is already shared between multiple strips. To minimize this effect, the SSAs can be programmed to effectively adjust the trigger arrival time by shifting the phase of the sampling clock. In figure 9 the efficiency of observing a reconstructed track in coincidence with a cluster in the DUT is shown as a function of this timing offset, in 3.125 ns steps. For the calculation of the efficiencies, here and elsewhere in this paper, only tracks that point towards the detector surface according to the alignment are considered. The scan is performed for a detection threshold of 4.8 ke⁻, an operating point with high signal efficiency and low noise (as will be discussed in section 5.4). The efficiency has a wide plateau and reaches 99.75%. In figure 10 the ratio of the number of clusters with two or more hits $N_{cl}^{>1}$ with respect to all clusters is shown as a function of the timing offset.

For all the studies in this paper the timing was fixed at the indicated working point, although it has slightly sub-optimal efficiency. The working point was chosen to maximize efficiency and cluster size based on results from online measurements using the Monicelli framework during data-taking. This online calculation, which uses a less precise geometric alignment of the DUT, inconsistently considered tracks just outside the actual sensor boundary when computing the efficiency. This inefficiency is enhanced when operating with high thresholds.
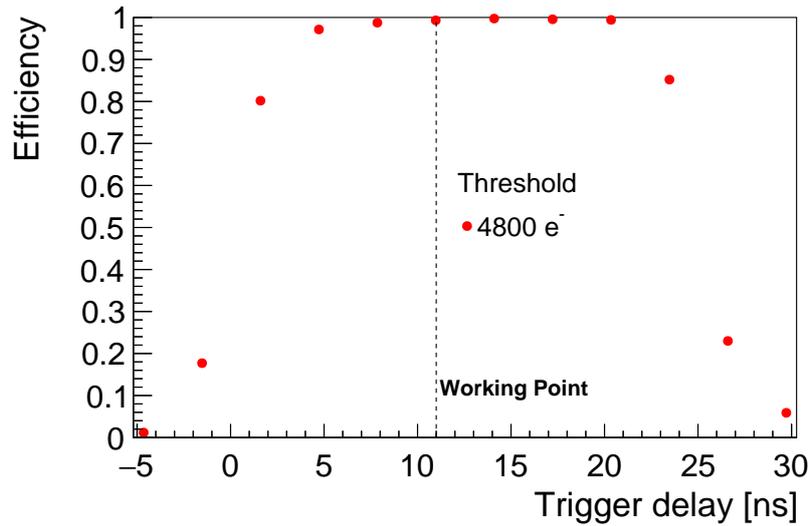

Figure 9. Efficiency as function of the delay of the trigger for a detection threshold of $4.8\,\mathrm{ke}^-$. The chosen working point is indicated by the dashed vertical line.
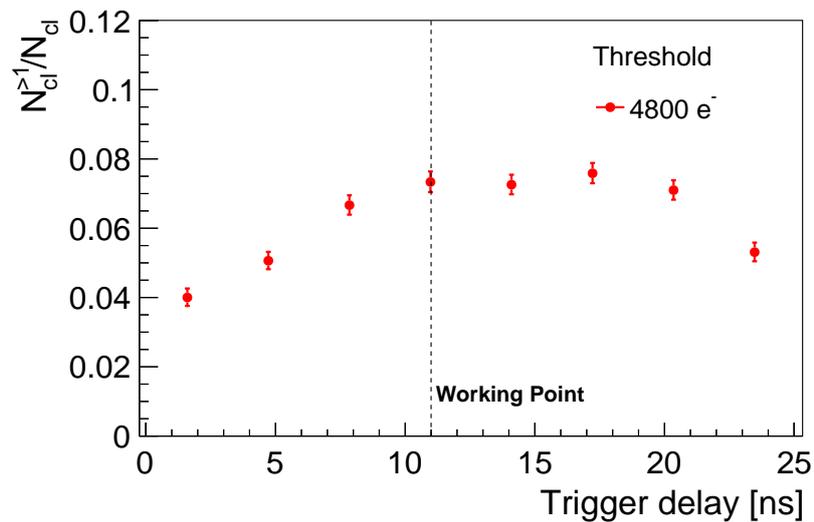

Figure 10. Fraction of clusters with more than one strip $N_{\mathrm{cl}}^{>1}/N_{\mathrm{cl}}$ as function of the delay of the trigger. The chosen working point is indicated by the dashed vertical line.
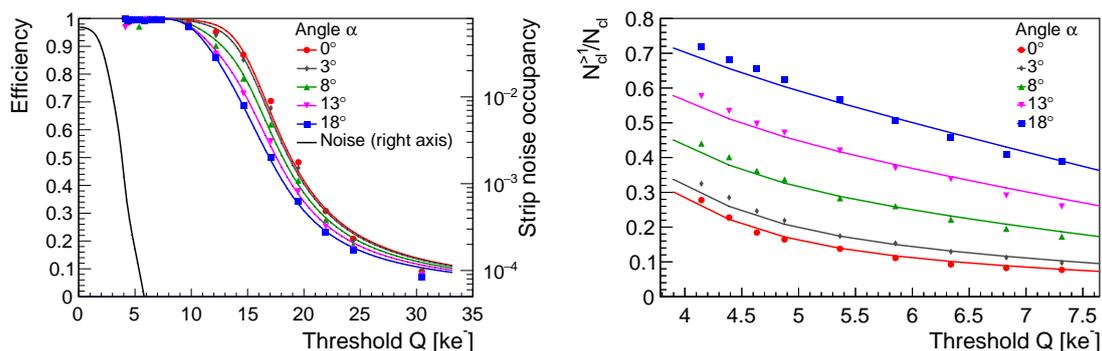
Figure 11. Left: efficiencies as functions of the threshold Q for various horizontal rotation angles α. The measured noise in the module is also shown. Right: fraction of clusters with more than one strip $N_{cl}^{>1}/N_{cl}$ as a function of Q for various horizontal rotation angles α. The measurements (points) are compared to the simulation (solid lines).

5.4 Efficiency and cluster size

The efficiency of the module is measured with respect to telescope tracks which point to the sensor, and hits are counted as matched if they are within $|\Delta x| = 200\,\mu m$ of the telescope track. Clusters not associated with a track are discarded. The efficiencies and the cluster sizes are determined as functions of the detection threshold value Q and the horizontal rotation angle α. The alignment is repeated each time the DUT is rotated, so that only telescope tracks crossing the sensor in its new position are considered in efficiency calculations. The results are shown in figure 11, left. The efficiency plateaus at 99.7% for detection thresholds up to $8\,\mathrm{ke}^-$, for all angles α. For higher thresholds the efficiency drops with a dependence on the particle angle of incidence. This behavior is expected as charge is distributed among several strips at oblique angles, so that the signals on individual strips are reduced and do not reach the threshold. The increased fraction of multi-strip clusters at higher angles is confirmed by a measurement of cluster sizes as a function of the threshold (figure 11, right). The fraction of clusters with two or more hits ($N_{cl}^{>1}/N_{cl}$) is always reduced for an increased threshold.

The simple model described in section 4 is fit to the measured efficiencies and the cluster sizes as functions of the threshold and rotation angle α. The parameters can be found in table 1. A decent qualitative description can be reached based on this simple model.

For each cluster the SSA provides additional information when the signal of at least one constituent hit exceeds a second higher HIP threshold. The selection performance of this second threshold and a comparison to the detection threshold is shown in figure 12. Overall, the HIP threshold behaves similarly to the main discriminator, though we observe a slightly lower efficiency at a given value of Q in this particular module (unlike the detection threshold, the HIP threshold cannot be tuned).

5.5 Resolution

The resolution of the sensor is determined for various values of the angle α. For these studies the detection threshold was set to $6.2\,\mathrm{ke}^-$. In figure 13 the residuals between the cluster position and the corresponding telescope track position are shown separately for one- and two-strip clusters. The distributions predicted by the model are convolved with a Gaussian distribution to account for the
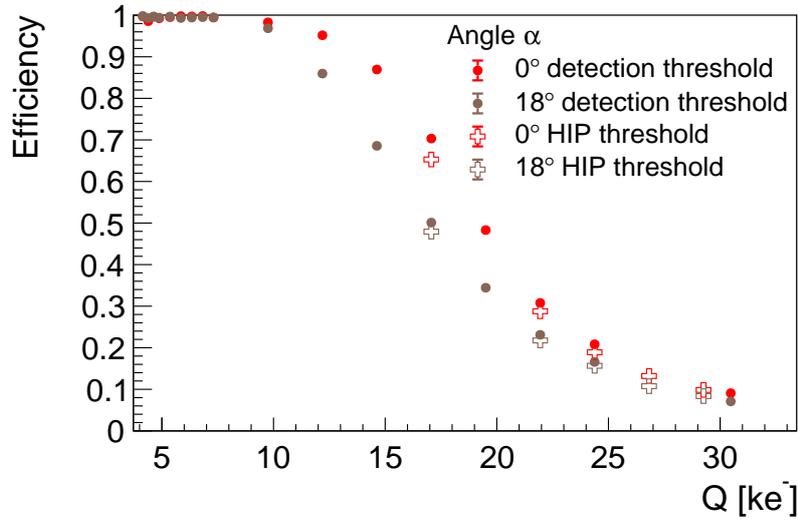
Figure 12. Comparison of the efficiencies as functions of the detection threshold (filled markers) and the HIP threshold (open markers), for two horizontal rotation angles α.

Figure 13. Residual between the telescope track and cluster positions for different angles α: 0° (top left), 3° (top right), 8° (bottom left) and 13° (bottom right). The data, shown with statistical errors, are fit with the model prediction (dashed lines) convolved with the telescope resolution (solid lines).

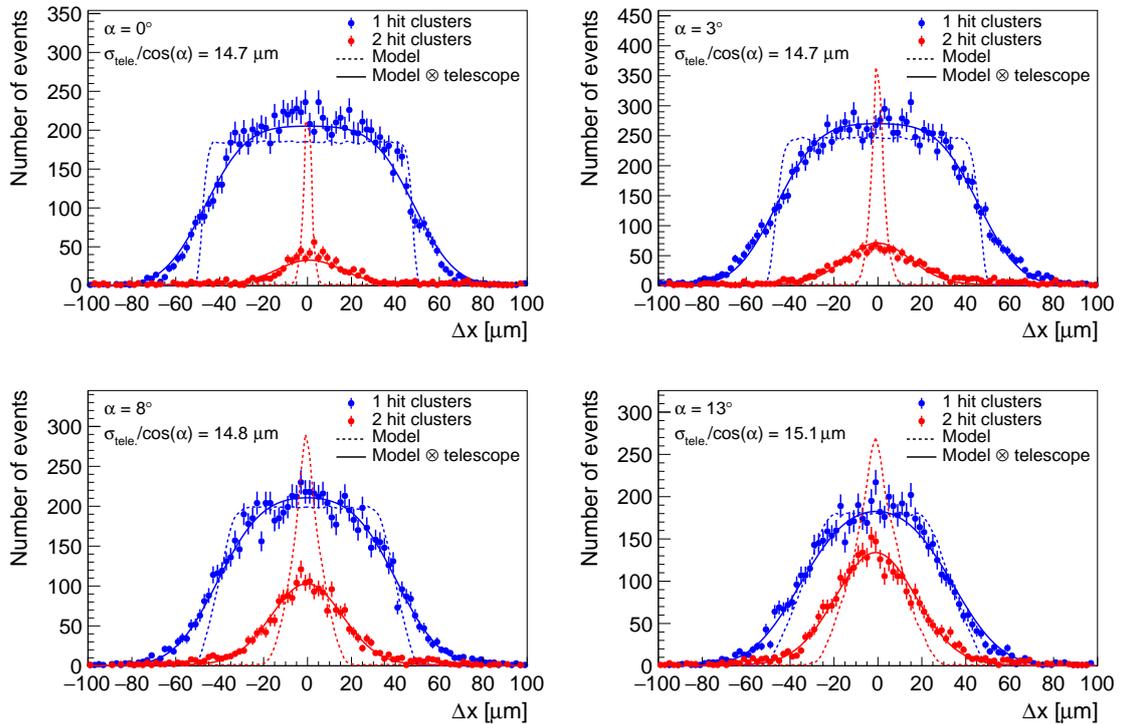effect of the telescope resolution (σ_{tele}). The width of the Gaussian (σ) depends on the angle α as $\sigma = \sigma_{\text{tele}}/\cos(\alpha)$. The value σ_{tele} is extracted by fitting the model (including the convolving resolution term) to the data for all angles. During this fit all other parameters of the simple model are fixed at their values determined in section 5.4. The resolution is found to be 14.7 µm, where this value corresponds to the resolution of the track position on the DUT when the sensor is parallel to the telescope planes ($\alpha = 0°$). The obtained predictions provide a good description of the data. In addition to this convolved prediction, the resolutions without the telescope term are also shown, corresponding to the simulated intrinsic resolution of the sensor only.

At $\alpha = 0°$ the two-strip clusters are located in a narrow region (around 10 µm) between the strip-implant boundaries, mainly determined by diffusion effects. With an increasing angle the chance of traversing two strips becomes geometrically enhanced. Therefore, the fraction of two-strip clusters increases. Conversely, clusters with just one strip are constrained to the center of the strips and their resolution is improved due to the effectively smaller pitch. The root mean square values (RMS) of the single-cluster residual distribution, with the effect of the telescope resolution removed, are 28, 27, 24, and 22 µm, for angles of $\alpha = 0°$, $3°$, $8°$ and $13°$ respectively. Similarly, the RMS of the two-cluster residual distributions are 10, 8, 8, and 9 µm, for angles of $\alpha = 0°$, $3°$, $8°$ and $13°$ respectively.

In figure 14 the efficiency is shown as a function of the interstrip position on the DUT sensor, with the position determined using the telescope. As in figure 13, we show the convolved model,
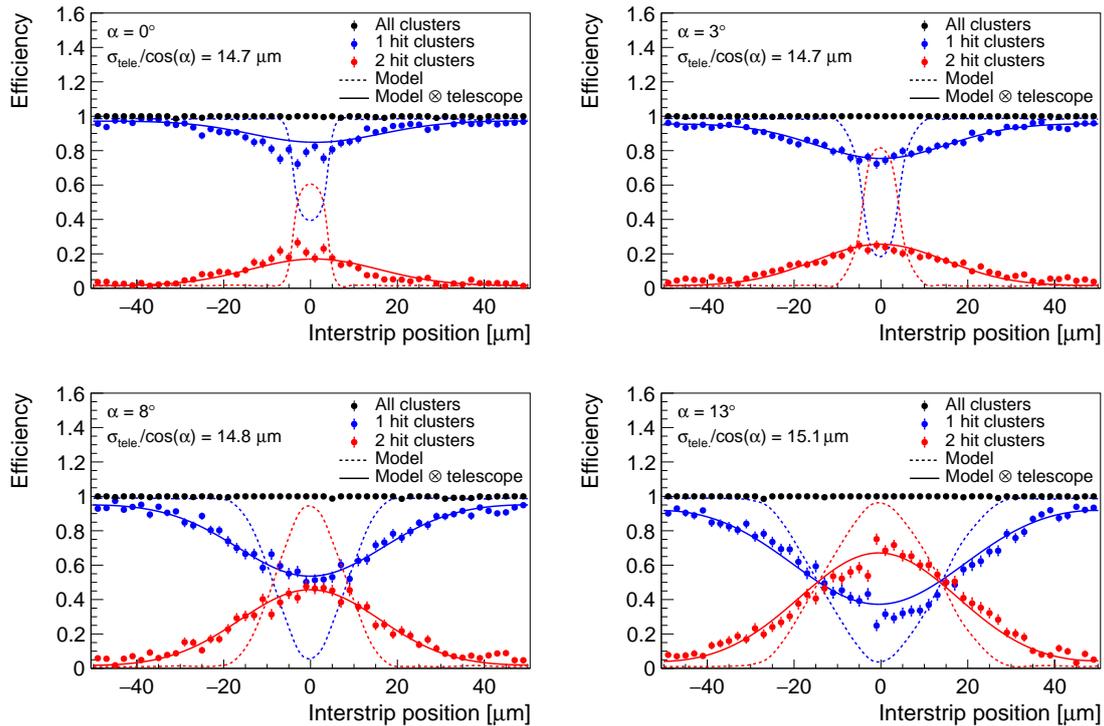
Figure 14. Distribution of the efficiency for interstrip positions of the telescope tracks at different horizontal rotation angles α: $0°$ (top left), $3°$ (top right), $8°$ (bottom left) and $13°$ (bottom right). The data, shown with statistical errors, are fit with the model prediction (dashed lines) convolved with the telescope resolution (solid lines). The border between two strips is at 0 µm, and the strip implants are centered at -50 µm and 50 µm.

taking into account the stated telescope resolution of 14.7 μm, and the simulated efficiency when the effect of the telescope is removed. The efficiency when considering all clusters is flat across the interstrip region and reaches 99.7%.

6 Conclusions

The SSA is one of the four front-end chips designed for the high luminosity upgrade of the CMS Outer Tracker. The performance of a prototype module consisting of two SSA chips connected to a sensor was studied at the Fermilab Test Beam Facility using 120 GeV protons. This 2×SSA module was constructed to closely approximate the sensor-ASIC configuration which will be used in the full PS module, and these measurements constitute the first published results of the SSA performance using a particle beam. The performance of the module was tested at incident beam angles between 0° and 18°. The module is shown to be fully efficient, at all angles for nominal particle detection thresholds, and the functionality of a second highly ionizing particle detecting threshold is confirmed. The results agree closely with a simple physical model of the protons interacting with the silicon strip sensor, including protons passing near the boundaries between sensor strips where clusters consisting of multiple hits are more likely to occur. This agreement, along with previous studies of the SSA [11, 22], validates the ASIC's front-end design, module prototype construction and the tracker DAQ software. SSAs will next be used in the construction of two-sensor modules for further tests of the PS module performance, in particular of the stub-formation logic.

References

[1] G. Apollinari, I. Béjar Alonso, O. Brüning, M. Lamont and L. Rossi, eds., *High-Luminosity Large Hadron Collider (HL-LHC): Preliminary Design Report*, Tech. Rep., CERN, Geneva (2015), CERN-2015-005, DOI: 10.5170/CERN-2015-005.

[2] CMS collaboration, *The CMS Experiment at the CERN LHC*, 2008 *JINST* **3** S08004.

[3] CMS collaboration, *Technical Proposal for the Phase-II Upgrade of the CMS Detector*, Tech. Rep., CERN, Geneva (2015), CERN-LHCC-2015-010, LHCC-P-008, CMS-TDR-15-02, DOI: 10.17181/CERN.VU8I.D59J.

[4] CMS collaboration, *The Phase-2 Upgrade of the CMS Tracker*, Tech. Rep., CERN, Geneva (2017), CERN-LHCC-2017-009, CMS-TDR-014, DOI: 10.17181/CERN.QZ28.FLHW.

[5] CMS collaboration, *The CMS trigger in Run 2*, *PoS* **EPS-HEP2017** (2017) 523.

[6] THE TRACKER GROUP OF THE CMS collaboration, *The CMS Phase-1 Pixel Detector Upgrade*, 2021 *JINST* **16** P02027 [arXiv:2012.14304].

[7] K. Uchida et al., *Results from the CBC3 readout ASIC for CMS 2S-modules*, *Nucl. Instrum. Meth. A* **924** (2019) 175.

[8] S.S. El Nasr-Storey, *Recent developments in the CBC3, a CMS micro-strip readout ASIC for track-trigger modules at the HL-LHC*, *Nucl. Instrum. Meth. A* **936** (2019) 278.

[9] D. Ceresa, J. Kaplon, R. Francisco, A. Caratelli, K. Kloukinas and A. Marchioro, *A 65 nm pixel readout ASIC with quick transverse momentum discrimination capabilities for the CMS Tracker at HL-LHC*, 2016 *JINST* **11** C01054.

[10] A. Caratelli, D. Ceresa, J. Kaplon, K. Kloukinas, Y. Leblebici, J. Murdzek et al., *Short-Strip ASIC (SSA): A 65nm silicon-strip readout ASIC for the Pixel-Strip (PS) module of the CMS Outer Tracker detector upgrade at HL-LHC*, *PoS* **TWEPP-17** (2018) 031.

[11] A. Caratelli, S. Scarfi, D. Ceresa, K. Kloukinas, J. Kaplon, J. De Clercq et al., *Characterization of the first prototype of the Silicon-Strip readout ASIC (SSA) for the CMS Outer-Tracker phase-2 upgrade*, *PoS* **TWEPP2018** (2019) 159.

[12] B. Nodari, G. Bergamin, L. Caponetto, A. Caratelli, D. Ceresa, J. De Clercq et al., *First results from the CIC data aggregation ASIC for the Phase 2 CMS Outer Tracker*, *PoS* **TWEPP2019** (2020) 102.

[13] J.M. Mendez, S. Baron, S. Kulis and J. Fonseca, *New LpGBT-FPGA IP: Simulation model and first implementation*, *PoS* **TWEPP2018** (2019) 059.

[14] CMS collaboration, *P-Type Silicon Strip Sensors for the new CMS Tracker at HL-LHC*, 2017 *JINST* **12** P06018.

[15] S. Kwan et al., *The Pixel Tracking Telescope at the Fermilab Test Beam Facility*, *Nucl. Instrum. Meth. A* **811** (2016) 162.

[16] M. Pesaresi, M. Barros Marin, G. Hall, M. Hansen, G. Iles, A. Rose et al., *The FC7 AMC for generic DAQ & control applications in CMS*, 2015 *JINST* **10** C03036.

[17] M. Haranko, *Development of a test DAQ system for the CMS Phase-2 outer tracker upgrade*, Ph.D. thesis, Hamburg University, Germany (2019).

[18] J.T. De Clercq, A. Caratelli, D. Ceresa, G. Galbit, M. Haranko, S. Jain et al., *OT-μDTC, a test bench for testing CMS Outer Tracker Phase-2 module prototypes*, *PoS* **EPS-HEP2019** (2020) 170.

[19] K. Biery, E. Flumerfelt, J. Freeman, W. Ketchum, G. Lukhanin and R. Rechenmacher, *artdaq: DAQ Software Development Made Simple*, *J. Phys. Conf. Ser.* **898** (2017) 032013.

[20] L. Landau, *On the energy loss of fast particles by ionization*, *J. Phys.* **8** (1944) 201.

[21] K.S. Kolbig and B. Schorr, *A Program Package for the Landau Distribution*, *Comput. Phys. Commun.* **31** (1984) 97 [*Erratum ibid.* **178** (2008) 972].

[22] D. Ceresa, G. Bergamin, A. Caratelli, J. Kaplon, K. Kloukinas, S. Scarfi et al., *MPA-SSA, design and test of a 65 nm ASIC-based system for particle tracking at HL-LHC featuring on-chip particle discrimination*, in proceedings of *IEEE Nuclear Science Symposium and Medical Imaging Conference*, Manchester, U.K., 26 October–2 November 2019, pp. 1–3.

The Tracker Group of the CMS collaboration

Institut für Hochenergiephysik, Wien, Austria

W. Adam, T. Bergauer, K. Damanakis, M. Dragicevic, R. Frühwirth[1], H. Steininger

Universiteit Antwerpen, Antwerpen, Belgium

W. Beaumont, D. Di Croce, X. Janssen, T. Kello, A. Lelek, P. Van Mechelen, S. Van Putte, N. Van Remortel

Vrije Universiteit Brussel, Brussel, Belgium

M. Delcourt, A. De Moor, J. D'Hondt, S. Lowette, A. Morton, D. Muller, A.R. Sahasransu, E. Sørensen Bols, D. Vannerom

Université Libre de Bruxelles, Bruxelles, Belgium

Y. Allard, B. Clerbaux, S. Dansana, G. De Lentdecker, W. Deng, L. Favart, D. Hohov, A. Khalilzadeh, K. Lee, M. Mahdavikhorrami, I. Makarenko, S. Paredes, N. Postiau, F. Robert, L. Thomas, M. Vanden Bemden, P. Vanlaer, H. Wang, Y. Yang

Université Catholique de Louvain, Louvain-la-Neuve, Belgium

A. Benecke, A. Bethani, G. Bruno, F. Bury, C. Caputo, P. David, A. Deblaere, C. Delaere, I.S. Donertas, A. Giammanco, S. Jain, V. Lemaitre, K. Mondal, J. Prisciandaro, N. Szilasi, A. Taliercio, M. Teklishyn, P. Vischia, S. Wertz

Institut Ruđer Bošković, Zagreb, Croatia

V. Brigljević, B. Chitroda, D. Ferenček, D. Majumder, S. Mishra, M. Roguljić, A. Starodumov[2], T. Šuša

Department of Physics, University of Helsinki, Helsinki, Finland

P. Eerola

Helsinki Institute of Physics, Helsinki, Finland

E. Brücken, T. Lampén, L. Martikainen, E. Tuominen

Lappeenranta-Lahti University of Technology, Lappeenranta, Finland

A. Karadzhinova-Ferrer, P. Luukka, H. Petrow, T. Tuuva[†]

Université de Strasbourg, CNRS, IPHC UMR 7178, Strasbourg, France

J.-L. Agram[3], J. Andrea, D. Apparu, D. Bloch, C. Bonnin, J.-M. Brom, E. Chabert, L. Charles, C. Collard, E. Dangelser, U. Goerlach, C. Grimault, L. Gross, C. Haas, M. Krauth, E. Nibigira, N. Ollivier-Henry, E. Silva Jiménez

Université de Lyon, Université Claude Bernard Lyon 1, CNRS/IN2P3, IP2I Lyon, UMR 5822, Villeurbanne, France

E. Asilar, G. Baulieu, G. Boudoul, L. Caponetto, N. Chanon, D. Contardo, P. Dené, T. Dupasquier, G. Galbit, N. Lumb[4], L. Mirabito, B. Nodari, M. Vander Donckt, S. Viret

RWTH Aachen University, I. Physikalisches Institut, Aachen, Germany

V. Botta, L. Feld, W. Karpinski, K. Klein, M. Lipinski, D. Louis, D. Meuser, A. Pauls, G. Pierschel, M. Rauch, N. Röwert, J. Schulz, M. Teroerde, M. Wlochal

RWTH Aachen University, III. Physikalisches Institut B, Aachen, Germany

C. Dziwok, G. Fluegge, O. Pooth, A. Stahl, T. Ziemons

Deutsches Elektronen-Synchrotron, Hamburg, Germany

S. Bhattacharya, F. Blekman[5], A. Campbell, C. Cheng, S. Consuegra Rodriguez, G. Eckerlin, D. Eckstein, E. Gallo[5], M. Guthoff, C. Kleinwort, R. Mankel, H. Maser, C. Muhl, A. Mussgiller, A. Nürnberg, Y. Otarid, O. Reichelt, M. Savitskyi, P. Schütze, R. Stever, N. Tonon[†], A. Velyka, A. Ventura Barroso, R. Walsh, Q. Wang, A. Zuber

University of Hamburg, Hamburg, Germany

M. Antonello, H. Biskop, P. Buhmann, P. Connor, F. Feindt[6], A. Froehlich, E. Garutti, M. Hajheidari, J. Haller, A. Hinzmann, H. Jabusch, G. Kasieczka, R. Klanner, V. Kutzner, J. Lange, T. Lange, S. Martens, M. Mrowietz, Y. Nissan, K. Pena, P. Schleper, J. Schwandt, G. Steinbrück, A. Tews, J. Wellhausen, I. Zoi

Institut für Experimentelle Teilchenphysik, KIT, Karlsruhe, Germany

M. Abbas, L. Ardila[7], M. Balzer[7], T. Barvich, B. Berger, E. Butz, M. Caselle[7], W. De Boer[†], A. Dierlamm[7], A. Droll, U. Elicabuk, F. Hartmann, U. Husemann, G. Kösker, R. Koppenhöfer, S. Maier, S. Mallows, T. Mehner[7], J.-O. Müller-Gosewisch, Th. Muller, M. Neufeld, O. Sander[7], I. Shvetsov, H. J. Simonis, P. Steck, L. Stockmeier, M. Wassmer, F. Wittig

Institute of Nuclear and Particle Physics (INPP), NCSR Demokritos, Aghia Paraskevi, Greece

G. Anagnostou, P. Assiouras, G. Daskalakis, I. Kazas, A. Kyriakis, D. Loukas

Wigner Research Centre for Physics, Budapest, Hungary

T. Balázs, M. Bartók, K. Márton, F. Siklér, V. Veszprémi

National Institute of Science Education and Research, HBNI, Bhubaneswar, India

S. Bahinipati[8], A.K. Das, P. Mal, T. Mishra, A. Nayak[9], D.K. Pattanaik, P. Saha, S.K. Swain

University of Delhi, Delhi, India

A. Bhardwaj, C. Jain, G. Jain, A. Kumar, K. Ranjan, S. Saumya

Saha Institute of Nuclear Physics, Kolkata, India

S. Baradia, R. Bhattacharya, S. Dutta, P. Palit, G. Saha, S. Sarkar

Indian Institute of Technology Madras, Madras, India

M. Alibordi, P.K. Behera, S. Chatterjee, G. Dash, P. Jana, P. Kalbhor, J. Libby, M. Mohammad, R. Pradhan, P.R. Pujahari, N.R. Saha, K. Samadhan, A. Sharma, A.K. Sikdar, S. Verma

INFN Sezione di Bari[a], Università di Bari[b], Politecnico di Bari[c], Bari, Italy

P. Cariola[a], D. Creanza[a,c], M. de Palma[a,b], G. De Robertis[a], A. Di Florio[a,c], L. Fiore[a], F. Loddo[a], I. Margjeka[a], M. Mongelli[a], S. My[a,b], L. Silvestris[a]

INFN Sezione di Catania[a], Università di Catania[b], Catania, Italy

S. Albergo[a,b], S. Costa[a,b], A. Di Mattia[a], R. Potenza[a,b], M.A. Saizu[a,10], A. Tricomi[a,b], C. Tuve[a,b]

INFN Sezione di Firenze[a], Università di Firenze[b], Firenze, Italy

G. Barbagli[a], G. Bardelli[a,b], M. Brianzi[a], B. Camaiani[a,b], A. Cassese[a], R. Ceccarelli[a,b], R. Ciaranfi[a], V. Ciulli[a,b], C. Civinini[a], R. D'Alessandro[a,b], F. Fiori[a,b], E. Focardi[a,b], G. Latino[a,b],

P. Lenzi^{a,b}, M. Lizzo^{a,b}, M. Meschini^a, S. Paoletti^a, A. Papanastassiou^{a,b}, R. Seidita^{a,b}, G. Sguazzoni^a, L. Viliani^a

INFN Sezione di Genova, Genova, Italy

P. Chatagnon, F. Ferro, E. Robutti

INFN Sezione di Milano-Bicocca^a, Università di Milano-Bicocca^b, Milano, Italy

F. Brivio^a, M.E. Dinardo^{a,b}, P. Dini^a, S. Gennai^a, L. Guzzi^{a,b}, S. Malvezzi^a, D. Menasce^a, L. Moroni^a, D. Pedrini^a, D. Zuolo^{a,b}

INFN Sezione di Padova^a, Università di Padova^b, Padova, Italy

P. Azzi^a, N. Bacchetta^a, P. Bortignon^{a,11}, D. Bisello^a, T. Dorigo^a, M. Tosi^{a,b}, H. Yarar^{a,b}

INFN Sezione di Pavia^a, Università di Bergamo^b, Bergamo, Università di Pavia^c, Pavia, Italy

L. Gaioni^{a,b}, M. Manghisoni^{a,b}, L. Ratti^{a,c}, V. Re^{a,b}, E. Riceputi^{a,b}, G. Traversi^{a,b}

INFN Sezione di Perugia^a, Università di Perugia^b, CNR-IOM Perugia^c, Perugia, Italy

P. Asenov^{a,c}, G. Baldinelli^{a,b}, F. Bianchi^{a,b}, G.M. Bilei^a, S. Bizzaglia^a, M. Caprai^a, B. Checcucci^a, D. Ciangottini^a, A. Di Chiaro^a, L. Fanò^{a,b}, L. Farnesini^a, M. Ionica^a, M. Magherini^{a,b}, G. Mantovani^{a,b}, V. Mariani^{a,b}, M. Menichelli^a, A. Morozzi^a, F. Moscatelli^{a,c}, D. Passeri^{a,b}, A. Piccinelli^{a,b}, P. Placidi^{a,b}, A. Rossi^{a,b}, A. Santocchia^{a,b}, D. Spiga^a, L. Storchi^a, T. Tedeschi^{a,b}, C. Turrioni^{a,b}

INFN Sezione di Pisa^a, Università di Pisa^b, Scuola Normale Superiore di Pisa^c, Pisa, Italy, Università di Siena^d, Siena, Italy

P. Azzurri^a, G. Bagliesi^a, A. Basti^a, R. Beccherle^a, L. Bianchini^{a,b}, T. Boccali^a, F. Bosi^a, R. Castaldi^a, M.A. Ciocci^{a,b}, V. D'Amante^{a,d}, R. Dell'Orso^a, S. Donato^a, A. Giassi^a, F. Ligabue^{a,c}, G. Magazzu^a, E. Manca^{a,c}, M. Massa^a, E. Mazzoni^a, A. Messineo^{a,b}, A. Moggi^a, M. Musich^{a,b}, F. Palla^a, S. Parolia^{a,b}, P. Prosperi^a, F. Raffaelli^a, G. Ramirez Sanchez^{a,c}, A. Rizzi^{a,b}, S. Roy Chowdhury^{a,c}, P. Spagnolo^a, R. Tenchini^a, G. Tonelli^{a,b}, A. Venturi^a, P.G. Verdini^a, S. Zagaria^a

INFN Sezione di Torino^a, Università di Torino^b, Torino, Italy

N. Bartosik^a, R. Bellan^{a,b}, S. Coli^a, M. Costa^{a,b}, R. Covarelli^{a,b}, G. Dellacasa^a, N. Demaria^a, S. Garbolino^a, S. Garrafa Botta^a, M. Grippo^{a,b}, F. Luongo^{a,b}, A. Mecca^{a,b}, E. Migliore^{a,b}, E. Monteil^{a,b}, G. Ortona^a, L. Pacher^{a,b}, F. Rotondo^a, A. Vagnerini^{a,b}

National Centre for Physics, Islamabad, Pakistan

A. Ahmad, M. Ahmad, M.I. Asghar, A. Awais, M.I.M. Awan, M. Saleh

Instituto de Física de Cantabria (IFCA), CSIC-Universidad de Cantabria, Santander, Spain

A. Calderón, J. Duarte Campderros, M. Fernandez, G. Gomez, F.J. Gonzalez Sanchez, R. Jaramillo Echeverria, C. Lasaosa, D. Moya, J. Piedra, A. Ruiz Jimeno, L. Scodellaro, I. Vila, A.L. Virto, J.M. Vizan Garcia

CERN, European Organization for Nuclear Research, Geneva, Switzerland

D. Abbaneo, I. Ahmed, E. Albert, J. Almeida, M. Barinoff, J. Batista Lopes, G. Bergamin^{12}, G. Blanchot, F. Boyer, A. Caratelli, R. Carnesecchi, D. Ceresa, J. Christiansen, K. Cichy, J. Daguin, S. Detraz, M. Dudek, N. Emriskova^{13}, F. Faccio, N. Frank, T. French, A. Hollos, J. Kaplon,

K. Kloukinas, N. Koss, L. Kottelat, D. Koukola, M. Kovacs, J. Lalic, A. La Rosa, P. Lenoir, R. Loos, A. Marchioro, A. Mastronikolis, I. Mateos Dominguez[14], S. Mersi, S. Michelis, A. Nookala, A. Onnela, S. Orfanelli, T. Pakulski, A. Papadopoulos[15], A. Perez, F. Perez Gomez, J.-F. Pernot, P. Petagna, Q. Piazza, Z. Pissaki, P. Rose, S. Scarfi[16], M. Sinani, R. Tavares Rego, P. Tropea, J. Troska, A. Tsirou, F. Vasey, P. Vichoudis, A. Zografos[17]

Paul Scherrer Institut, Villigen, Switzerland

W. Bertl[†], L. Caminada[18], A. Ebrahimi, W. Erdmann, R. Horisberger, H.-C. Kaestli, D. Kotlinski, C. Lange, U. Langenegger, B. Meier, M. Missiroli[18], L. Noehte[18], T. Rohe, S. Streuli

Institute for Particle Physics, ETH Zurich, Zurich, Switzerland

K. Androsov, M. Backhaus, R. Becker, P. Berger, A. Calandri, A. de Cosa, D. di Calafiori, L. Djambazov, M. Donega, C. Dorfer, F. Eble, F. Glessgen, C. Grab, D. Hits, W. Lustermann, M. Meinhard, J. Niedziela, V. Perovic, M. Reichmann, B. Ristic, U. Roeser, D. Ruini, J. Sörensen, R. Wallny

Universität Zürich, Zurich, Switzerland

P. Bärtschi, K. Bösiger, D. Brzhechko, F. Canelli, K. Cormier, R. Del Burgo, A. De Wit, M. Huwiler, W. Jin, A. Jofrehei, B. Kilminster, S. Leontsinis, S.P. Liechti, A. Macchiolo, R. Maier, V. Mikuni, U. Molinatti, I. Neutelings, A. Reimers, P. Robmann, S. Sanchez Cruz, Y. Takahashi, D. Wolf

National Taiwan University (NTU), Taipei, Taiwan

P.-H. Chen, W.-S. Hou, R.-S. Lu

University of Bristol, Bristol, United Kingdom

E. Clement, D. Cussans, J. Goldstein, S. Seif El Nasr-Storey, N. Stylianou

Rutherford Appleton Laboratory, Didcot, United Kingdom

J.A. Coughlan, K. Harder, M.-L. Holmberg, K. Manolopoulos, T. Schuh, I.R. Tomalin

Imperial College, London, United Kingdom

R. Bainbridge, J. Borg, C. Brown, G. Fedi, G. Hall, D. Monk, D. Parker, M. Pesaresi, K. Uchida

Brunel University, Uxbridge, United Kingdom

K. Coldham, J. Cole, M. Ghorbani, A. Khan, P. Kyberd, I.D. Reid

The Catholic University of America, Washington DC, U.S.A.

R. Bartek, A. Dominguez, R. Uniyal, A.M. Vargas Hernandez

Brown University, Providence, U.S.A.

G. Benelli, B. Burkle, X. Coubez, U. Heintz, N. Hinton, J. Hogan[19], A. Honma, A. Kent, A. Korotkov, D. Li, M. Lukasik, M. Narain, N. Pervan, S. Sagir[20], F. Simpson, E. Spencer, E. Usai, W.Y. Wong, W. Zhang

University of California, Davis, Davis, U.S.A.

E. Cannaert, M. Chertok, J. Conway, G. Haza, D. Hemer, F. Jensen, J. Thomson, W. Wei, T. Welton, R. Yohay[21], F. Zhang

University of California, Riverside, Riverside, U.S.A.

G. Hanson, W. Si

University of California, San Diego, La Jolla, U.S.A.

P. Chang, S.B. Cooperstein, R. Gerosa, L. Giannini, S. Krutelyov, B.N. Sathia, V. Sharma, M. Tadel, A. Yagil

University of California, Santa Barbara - Department of Physics, Santa Barbara, U.S.A.

V. Dutta, J. Incandela, M. Kilpatrick, S. Kyre, P. Masterson, M. Quinnan

University of Colorado Boulder, Boulder, U.S.A.

J.P. Cumalat, W.T. Ford, A. Hassani, G. Karathanasis, E. MacDonald, A. Perloff, C. Savard, N. Schonbeck, K. Stenson, K.A. Ulmer, S.R. Wagner, N. Zipper

Cornell University, Ithaca, U.S.A.

J. Alexander, S. Bright-Thonney, X. Chen, J. Conway, D. Cranshaw, J. Fan, X. Fan, A. Filenius, S. Hogan, P. Kotamnives, S. Lantz, J. Monroy, H. Postema, J. Reichert, M. Reid, D. Riley, A. Ryd, K. Smolenski, C. Strohman, J. Thom, P. Wittich, R. Zou

Fermi National Accelerator Laboratory, Batavia, U.S.A.

A. Bakshi, D.R. Berry, K. Burkett, D. Butler, A. Canepa, G. Derylo, J. Dickinson, K.F. Di Petrillo, A. Ghosh, C. Gingu, H. Gonzalez, S. Grünendahl, L. Horyn, M. Johnson, P. Klabbers, C.M. Lei, R. Lipton, S. Los, P. Merkel, S. Nahn, F. Ravera, L. Ristori, R. Rivera, L. Spiegel, L. Uplegger, E. Voirin, H.A. Weber

University of Illinois at Chicago (UIC), Chicago, U.S.A.

H. Becerril Gonzalez, S. Dittmer, A. Evdokimov, O. Evdokimov, C.E. Gerber, D.J. Hofman, C. Mills, T. Roy, S. Rudrabhatla, J. Yoo

The University of Iowa, Iowa City, U.S.A.

M. Alhusseini, S. Durgut, J. Nachtman, Y. Onel, C. Rude, C. Snyder, K. Yi[22]

Johns Hopkins University, Baltimore, U.S.A.

O. Amram, N. Eminizer, A. Gritsan, S. Kyriacou, P. Maksimovic, C. Mantilla Suarez, J. Roskes, M. Swartz, T. Vami

The University of Kansas, Lawrence, U.S.A.

J. Anguiano, A. Bean, R. Salvatico, C. Smith, G. Wilson

Kansas State University, Manhattan, U.S.A.

A. Ivanov, A. Modak, R. Taylor

University of Nebraska-Lincoln, Lincoln, U.S.A.

K. Bloom, D.R. Claes, C. Fangmeier, F. Golf, C. Joo, I. Kravchenko, J. Siado

State University of New York at Buffalo, Buffalo, U.S.A.

I. Iashvili, A. Kharchilava, C. McLean, D. Nguyen, J. Pekkanen, S. Rappoccio

Boston University, Boston, U.S.A.

A. Albert, Z. Demiragli, D. Gastler, E. Hazen, A. Peck, J. Rohlf

Northeastern University, Boston, U.S.A.

J. Li, A. Parker, L. Skinnari

Northwestern University, Evanston, U.S.A.

K. Hahn, Y. Liu, K. Sung

The Ohio State University, Columbus, U.S.A.

A. Basnet, C.S. Hill, K. Wei, B. Winer, B. Yates

University of Puerto Rico, Mayaguez, U.S.A.

S. Malik, S. Norberg, J.E. Ramirez Vargas

Purdue University, West Lafayette, U.S.A.

R. Chawla, S. Das, M. Jones, A. Jung, A. Koshy, M. Liu, G. Negro, J. Thieman

Purdue University Northwest, Hammond, U.S.A.

T. Cheng, J. Dolen, N. Parashar

Rice University, Houston, U.S.A.

K.M. Ecklund, S. Freed, A. Kumar, T. Nussbaum

University of Rochester, Rochester, U.S.A.

R. Demina, J. Dulemba, O. Hindrichs, S. Korjenevski

Rutgers, The State University of New Jersey, Piscataway, U.S.A.

Y. Gershtein, E. Halkiadakis, A. Hart, C. Kurup, A. Lath, K. Nash, M. Osherson, S. Schnetzer,
R. Stone, C. Xia

University of Tennessee, Knoxville, U.S.A.

S. Fiorendi, T. Holmes, L. Lee, S. Spanier

Texas A&M University, College Station, U.S.A.

R. Eusebi

Vanderbilt University, Nashville, U.S.A.

P. D'Angelo, W. Johns

†: Deceased
1: Also at Vienna University of Technology, Vienna, Austria
2: Also at Institute for Theoretical and Experimental Physics, Moscow, Russia
3: Also at Université de Haute-Alsace, Mulhouse, France
4: Now at Centre de Physique des Particules de Marseille (CPPM), Marseille, France
5: Also at University of Hamburg, Hamburg, Germany
6: Now at Deutsches Elektronen Synchrotron, Hamburg, Germany
7: Also at Institute for Data Processing and Electronics, KIT, Karlsruhe, Germany
8: Also at Indian Institute of Technology, Bhubaneswar, India
9: Also at Institute of Physics, HBNI, Bhubaneswar, India
10: Also at Horia Hulubei National Institute of Physics and Nuclear Engineering (IFIN-HH), Bucharest,
Romania
11: Also at University of Cagliari, Cagliari, Italy
12: Also at Institut Polytechnique de Grenoble, Grenoble, France
13: Also at Université de Strasbourg, CNRS, IPHC UMR 7178, Strasbourg, France

14: Also at Universidad de Castilla-La-Mancha, Ciudad Real, Spain

15: Also at University of Patras, Patras, Greece

16: Also at École Polytechnique Fédérale de Lausanne, Lausanne, Switzerland

17: Also at National Technical University of Athens, Athens, Greece

18: Also at Universität Zürich, Zurich, Switzerland

19: Now at Bethel University, St. Paul, Minnesota, U.S.A.

20: Now at Karamanoglu Mehmetbey University, Karaman, Turkey

21: Now at Florida State University, Tallahassee, U.S.A.

22: Also at Nanjing Normal University, Nanjing, China